Applied Physics Letters

Quantitative X-ray dark-field and phase tomography using single directional speckle scanning technique

Cite as: Appl. Phys. Lett. **108**, 124102 (2016); https://doi.org/10.1063/1.4944462
Submitted: 22 December 2015 • Accepted: 01 March 2016 • Published Online: 21 March 2016

Hongchang Wang, Yogesh Kashyap and Kawal Sawhney

Quantitative X-ray dark-field and phase tomography using single directional speckle scanning technique

Hongchang Wang,[a] Yogesh Kashyap, and Kawal Sawhney
Diamond Light Source, Harwell Science and Innovation Campus, Didcot, Oxfordshire OX11 0DE, United Kingdom

(Received 22 December 2015; accepted 1 March 2016; published online 21 March 2016)

X-ray dark-field contrast tomography can provide important supplementary information inside a sample to the conventional absorption tomography. Recently, the X-ray speckle based technique has been proposed to provide qualitative two-dimensional dark-field imaging with a simple experimental arrangement. In this letter, we deduce a relationship between the second moment of scattering angle distribution and cross-correlation degradation of speckle and establish a quantitative basis of X-ray dark-field tomography using single directional speckle scanning technique. In addition, the phase contrast images can be simultaneously retrieved permitting tomographic reconstruction, which yields enhanced contrast in weakly absorbing materials. Such complementary tomography technique can allow systematic investigation of complex samples containing both soft and hard materials.

[http://dx.doi.org/10.1063/1.4944462]

X-ray Computed Tomography (CT) allows visualizing the internal structure of a sample, and distinctive features can be clearly seen from absorption contrast if the elemental composition and density vary significantly. In combination with the absorption imaging, X-ray dark-field imaging can reveal subtle details and provide complementary scattering information from the samples. In addition, X-ray phase-contrast CT is superior to absorption CT in terms of higher sensitivity and possible lower radiation dose especially for weakly absorbing samples such as tumors in soft tissues. Over the past two decades, there has been a revolution in X-ray imaging, various X-ray dark-field, and phase imaging techniques, such as analyzer-, propagation-, and grating-based, and edge-illumination techniques, have been developed.[1–8] Fascinating achievements have been made to extend the phase and/or dark-field contrast imaging techniques from radiography to tomography.[9–14] For example, X-ray phase and dark-field CT has been used for in-depth study of breast, lung, brain, and even concrete.[15–18] Meanwhile, significant progress has been made to further improve the spatial resolution and reduce the delivered radiation dose of these techniques.[19–21] Nevertheless, the stringent requirements for the precision optics, mechanical stability, and X-ray beam conditions still limit the widespread and practical application of most existing techniques. Even though the propagation-based method does not require any specific optics, requirements on parameters such as spatial coherence, detector resolution, and the distance from the detector to sample are quite demanding.[22] In contrast, a new type of X-ray imaging technique based on the near-field speckle can circumvent these limitations by simply shining X-ray through a piece of filter membrane or abrasive paper.[23,24] The phase tomography has been demonstrated with a speckle tracking technique;[25] however, for the existing speckle based approaches, the dark-field signal cannot be directly used for quantitative tomographic reconstruction since it is not expressible as line integrals.[25] In addition, the spatial resolution of existing speckle tracking technique is relatively poor since it is limited to the speckle subset size (over ten pixels around a given pixel).[23,24] Although efforts have been made to improve the spatial resolution by applying 2D raster scans,[26] it is too time consuming.[27] To overcome such drawbacks, an advanced X-ray speckle scanning technique has been recently developed by scanning an abrasive paper transverse to the beam along a single direction.[28] In order to perform the X-ray dark-field tomography by using conventional CT reconstruction algorithms, the dark-field signal for each projection has to fulfill line integrals. X-ray dark-field imaging, based on small-angle scattering of X-rays, reflects broadening of the ray and can be quantitatively evaluated in terms of second moment of scattering angle distribution.[14,29,30] In this paper, we show how the second moment of scattering angle distribution can be related to the cross-correlation degradation of speckle and present quantitative 3D tomographic reconstruction of dark-field and phase signals. Importantly, the spatial resolution for X-ray dark-field and phase CT has improved from previous tens of pixels down to a single pixel size.

We first describe how to retrieve the phase shift and dark-field signal for each projection before carrying out the quantitative 3D reconstruction. For the single directional speckle scanning technique, a stack of reference speckle images is first collected with sample out of the beam by scanning the abrasive paper with a fixed step size μ perpendicular to the X-rays. The same procedure is repeated to collect the sample speckle images for each projection, once the sample is inserted into the beam. In order to derive quantitative relations, let $f(\eta, \rho)$ and $g(\eta, \rho)$ be the extracted speckle signal in the absence and presence of the sample at detector pixel (l, m). As illustrated in Fig. 1, η is scan steps of the single scanning process (horizontal) and ρ is orthogonal to the scan direction (vertical). For each projection, the cross-correlation

[a]Author to whom correspondence should be addressed. Electronic mail: hongchang.wang@diamond.ac.uk

coefficient γ between these two signals at detector pixel (l,m) with global translation (η_0,ρ_0) is given by following expression:

$$\gamma(\eta_0,\rho_0)_{l,m}=\sum_{\eta,\rho} f(\eta,\rho)_{l,m} g^*(\eta-\eta_0,\rho-\rho_0)_{l,m}. \quad (1)$$

Dropping the pixel subscripts to aid clarity, Eq. (1) can be rewritten in terms of Fourier components as[31]

$$\gamma(\eta_0,\rho_0)=\sum_{p,q}\tilde{f}(p,q)\tilde{g}^*(p,q)\exp\left[i2\pi\left(\frac{p\eta_0}{M}+\frac{q\rho_0}{N}\right)\right], \quad (2)$$

where (p,q) are Fourier space variables, M and N are the matrix size along η and ρ directions; (*) denotes complex conjugation; the operator $\tilde{}$ denotes the Fourier transform. If the field correlation function is taken as incoherent illumination,[26] the speckle intensity pattern $g(\eta,\rho)$ in the presence of the sample can be considered as convolution of $f(\eta,\rho)$ and the scattering angle distribution function $h(\eta,\rho,\upsilon_\eta,\upsilon_\rho,\sigma_\eta,\sigma_\rho)$ and written as follows:

$$g(\eta,\rho)=f(\eta,\rho)*h(\eta,\rho,\upsilon_\eta,\upsilon_\rho,\sigma_\eta^2,\sigma_\rho^2). \quad (3)$$

Here, $(\upsilon_\eta,\upsilon_\rho)$ is the displacement between two speckle patterns $f(\eta,\rho)$ and $g(\eta,\rho)$ and σ_η^2, σ_ρ^2 represent second moment of scattering angle distribution along these respective directions. The second moment of a scattering angle distribution reflects the broadening of the ray, and it can be defined as $\sigma_{\eta,\rho}^2=\int\Delta\theta_S^2 h(\Delta\theta_S)d\Delta\theta_S$ with $\Delta\theta_S$ representing the scattering angle. With the small angle approximation, the scattering angle distribution function can be written in terms of Gaussian distribution and expressed as

$$h(\eta,\rho,\upsilon_\eta,\upsilon_\rho,\sigma_\eta,\sigma_\rho)=A\exp\left[-\frac{1}{2\sigma_\eta^2}\left(\frac{\eta-\upsilon_\eta}{L_3}\right)^2-\frac{1}{2\sigma_\rho^2}\left(\frac{\rho-\upsilon_\rho}{L_3}\right)^2\right], \quad (4)$$

where L_3 represent the distance between the sample and the detector, and A is the intensity scale factor related to the transmission of the sample. Now, using convolution theorem of Fourier transform,[32] Eq. (3) can be expressed as follows:

$$\tilde{g}(p,q)=A\tilde{f}(p,q)\exp\left[-2\pi^2{L_3}^2\left(\sigma_\eta^2p^2+\sigma_\rho^2q^2\right)\right]\times\exp\left[-i2\pi\left(\frac{p\upsilon_\eta}{M}+\frac{q\upsilon_\rho}{N}\right)\right]. \quad (5)$$

Taking Eq. (5) into account, Eq. (2) can be rewritten as

$$\gamma(\eta_0,\rho_0)=A\sum_{p,q}\exp\left[-2\pi^2{L_3}^2\left(\sigma_\eta^2p^2+\sigma_\rho^2q^2\right)\right]\times|\tilde{f}(p,q)|^2\exp\left[i2\pi\left(\frac{p(\eta_0-\upsilon_\eta)}{M}+\frac{q(\rho_0-\upsilon_\rho)}{N}\right)\right]. \quad (6)$$

The maximum in the cross-correlation map would be at the point where two speckle images are best aligned with $\eta_0=\upsilon_\eta$ and $\rho_0=\upsilon_\rho$, and it can be written as

$$\gamma(\upsilon_\eta,\upsilon_\rho)^{\max}=A\sum_{p,q}|\tilde{f}(p,q)|^2\exp\left[-2\pi^2{L_3}^2(\sigma_\eta^2p^2+\sigma_\rho^2q^2)\right]\approx A|\tilde{f}(p_0,q_0)|^2\exp\left[-2\pi^2{L_3}^2(\sigma_\eta^2p_0^2+\sigma_\rho^2q_0^2)\right], \quad (7)$$

where frequencies p_0 and q_0 correspond to the maximum of the power spectrum $|\tilde{f}(p_0,q_0)|^2$, and they are related to the average speckle size $\bar{\varsigma}$, which is defined as

$$\bar{\varsigma}\equiv 2\pi/p_0=\kappa 2\pi/q_0. \quad (8)$$

Here, κ is related to asymmetrical nature of speckles in two different directions. Using normalized cross-correlation, the scaling factor $A|\tilde{f}(p_0,q_0)|^2$ will be unity and thus $\gamma(\upsilon_\eta,\upsilon_\rho)^{\max}$ can be simplified as

$$\gamma(\upsilon_\eta,\upsilon_\rho)^{\max}\approx\exp\left(\frac{-8\pi^4{L_3}^2\left(\sigma_\eta^2+\kappa^2\sigma_\rho^2\right)}{\bar{\varsigma}^2}\right)\equiv\exp\left(\frac{-8\pi^4{L_3}^2\sigma^2}{\bar{\varsigma}^2}\right). \quad (9)$$

σ^2 is the effective second moment of scattering angle distribution.[28] It may be noted that directional information can still be obtained from the same data set by analyzing the speckle pattern between the nearby pixels along the scan direction.[33] The dark-field signal D, defined in terms of the second moment of the scattering angle distribution,[29] can be written as follows:

$$D\equiv\sigma^2\approx\frac{-\bar{\varsigma}^2}{8\pi^4{L_3}^2}\ln\gamma(\upsilon_\eta,\upsilon_\rho)^{\max}. \quad (10)$$

Eq. (10) quantitatively describes the relation between second moment of the scattering angle distribution and degradation of parameter $\gamma_{l,m}^{\max}$. The speckle displacement $(\upsilon_\eta,\upsilon_\rho)$ can be retrieved by evaluating shifts in maximum of the cross-correlation map. For 1D scanning case, the first derivative of the sample's phase shift Φ along two orthogonal directions can then be calculated using the following relation:[28,34]

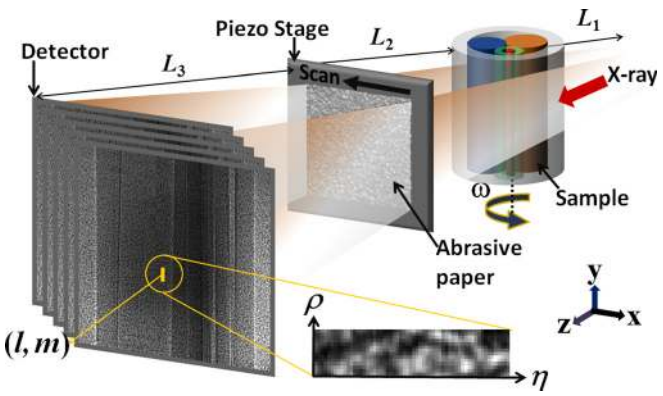

FIG. 1. Schematic representation of the experiment setup (not to scale). For each projection, a stack of speckle images is recorded using an X-ray detector by scanning abrasive paper transversely (along x direction) to the X-ray beam. For each pixel (l,m) of the detector, the speckle patterns without/with sample $f(\eta,\rho)/g(\eta,\rho)$ are obtained as function of η (scan steps) and ρ (orthogonal to the scan direction). From those speckle patterns, the differential phase and dark-field signals are retrieved.

$$\begin{cases} \dfrac{\partial \Phi}{\partial x} = \dfrac{2\pi}{\lambda} \dfrac{\upsilon_\eta \Gamma \mu}{L_3} \\ \dfrac{\partial \Phi}{\partial y} = \dfrac{2\pi}{\lambda} \dfrac{\upsilon_\rho P}{L_3}, \end{cases} \tag{11}$$

where μ and P are the scanning step size and detector's pixel size, respectively, and λ is the wavelength. Here, Γ is the geometrical magnification $\Gamma = (L_1 + L_2 + L_3)/L_1$. L_1 and L_2 represent the distances between the source, abrasive paper, and sample. The sample's integrated phase shift Φ can be calculated from above phase gradient, and can be related as line integral of the refractive index decrement δ. Meanwhile, the second moment of the scattering angle distribution σ^2 can be expressed as integral of the linear scattering coefficient ε, which is a material dependent variable describing the scattering parameter per unit length.[14] Hence, the phase shift and dark-field signal can be written as

$$\begin{cases} \Phi = \dfrac{2\pi}{\lambda} \displaystyle\int \delta(z) dz \\ \sigma^2 = \displaystyle\int \varepsilon(z) dz = \int \frac{\rho_n(z) \sigma_S(z)}{2\alpha} dz, \end{cases} \tag{12}$$

where ρ_n is the sample density, σ_S is the scattering cross-section, and α is the angular beam-broadening.[29] Since both Φ and σ^2 fulfill the line integral criteria, three-dimensional (3D) quantitative X-ray phase and dark-field computed tomography using conventional reconstruction methods become feasible. Therefore, both refractive index decrement δ and linear scattering coefficient ε can be quantitatively reconstructed simultaneously.[14,29,30] It should be noted that the above deduction is valid for both 1D and 2D speckle scanning approach. Since it is too time consuming to perform 2D raster scan, we only validated the proposed method using 1D scanning data for tomography.

As shown in Fig. 1, the experimental setup involves the sample, an X-ray area detector and a piece of abrasive paper. The experiment was performed on the Test beamline B16 at Diamond Light Source.[35] A monochromatic beam produced by a double crystal monochromator at an X-ray energy of 15 keV was used. The samples were mounted on a vertical axis rotation stage, which was located at a distance of $L_1 = 47$ m from the source. A sheet of silicon carbide abrasive paper (P3000) was mounted $L_2 = 0.20$ m downstream of the sample. The distance between the abrasive paper and the detector was set to the maximum mechanically achievable length of $L_3 = 1.09$ m in order to improve the sensitivity. The speckle pattern was recorded with an X-ray camera, which was based on a PCO 4000 CCD detector coupled with three microscope objectives. For the data presented in Figs. 2 and 4, a 10× microscope objective was selected with the effective pixel size of 1.8 μm × 1.8 μm with 2 × 2 binning, and the resolution is approximately 3.6 μm. In order to increase the field of view, a 4× microscope objective was used for the data shown in Fig. 3, and the effective pixel size is 9 μm × 9 μm with 4 × 4 binning. For each projection, a stack of 40 speckle images was taken as abrasive paper was scanned along single direction (horizontally) using a piezo stage. The scanning step size was $\mu = 1.8$ μm, and the exposure time for each image was 2 s.

First, we present the multimodal radiograph images of a fish eyeball (sprat) to show the advantage of the 1D speckle scanning technique compared with the conventional speckle tracking technique. Fig. 2 shows results for the X-ray horizontal and vertical wavefront gradients, dark-field, and phase images for the fish eyeball analyzed with the two techniques. To trace the speckle displacement at each pixel position for the speckle tracking technique, the subset with 20 × 20 surrounding pixels was chosen as a tradeoff between the spatial resolution and tracking accuracy. As shown in Figs. 2(a) and 2(b),

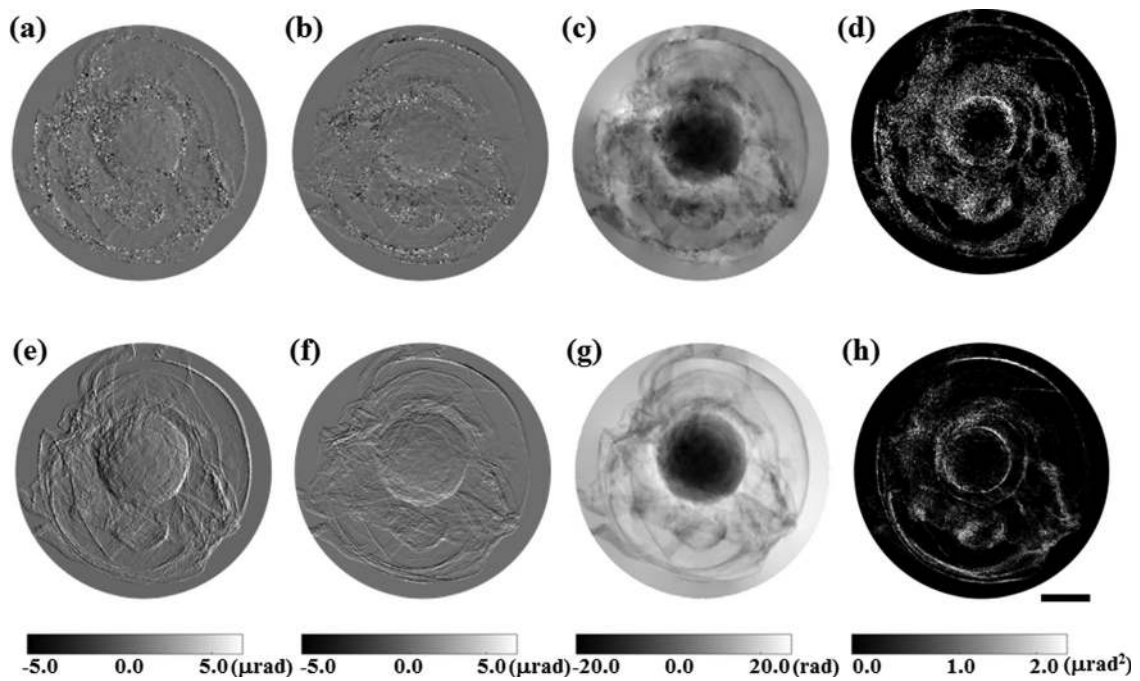

FIG. 2. (a) Vertical and (b) horizontal wavefront gradients, (c) phase-contrast, (d) dark-field images of a fish eyeball (sprat) obtained with the speckle tracking technique. (e)–(h) are the counterpart images obtained with the single direction speckle scanning technique. The scale bar at the bottom right corner of each image is 1 mm long.

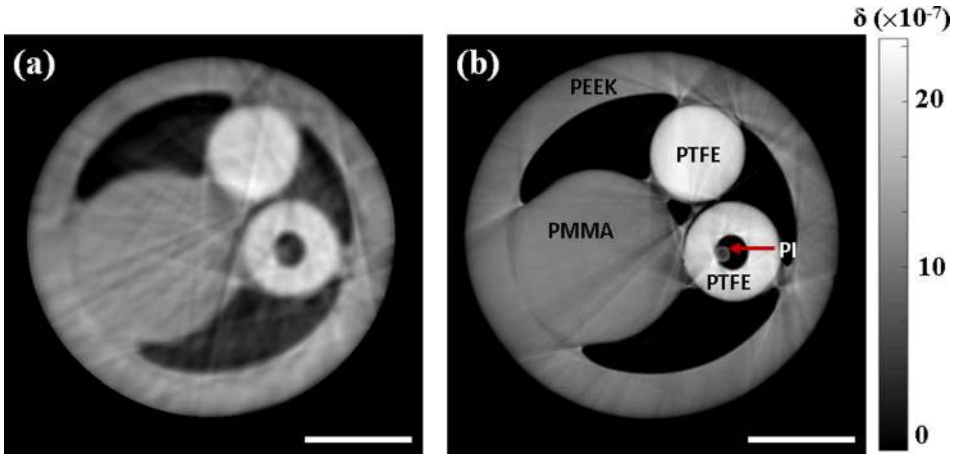

FIG. 3. Reconstructed phase contrast axial slices from tomographic reconstruction of tube and rod phantom using (a) speckle tracking and (b) single direction speckle scanning technique. The scale bar at the bottom right corner is 1 mm long.

artefacts arise for the areas where the wavefront gradients change abruptly. The quality of phase image in Fig. 2(c) is deteriorated due to the poor spatial resolution. In contrast, high quality images with significantly improved spatial resolution was retrieved by using the speckle scanning technique described in the previous paragraph, and all the fine features of the fish eyeball can be easily resolved (Figs. 2(e)–2(g)). Similarly, subtle details can be distinctly observed in dark-field image in Fig. 2(h) compared to the one in Fig. 2(d), and the dark-field image provides important complementary information to the absorption and phase images. Thus, two major drawbacks, namely, poor spatial resolution and unwanted artefacts, can be avoided; as a result, high angular sensitivity can be easily achieved by use of the 1D scanning approach.[34]

We have carried out further experiments on a simple phantom consisting of tubes and rods to demonstrate the improved high spatial resolution of the tomographic images. A set of 360 projection images with orientation angles ranging from 0° to 180° were collected. The reconstructed phase shift image is generally described as line integral of the refractive index decrement, and it can be directly used in tomography reconstruction using conventional reconstruction algorithm. However, the reconstructed phase errors contain low frequency noises and artefacts, which will propagate to the reconstructed volume if the conventional back projection technique is used. To avoid this, the Hilbert filter algorithm was used to reconstruct the refractive index decrement using the horizontal differential phase images.[9] The dark-field image corresponds to the line integral of scattering power,[30] and the Ram-Lak filter was used for dark-field reconstruction.[15]

Fig. 3 shows one reconstructed phase slice of the tube and rod phantom using the above two techniques obtained by scanning the abrasive paper along horizontal direction only. The phantom is composed of a Polyetheretherketone (PEEK) tube, a Polymethylmethacrylate (PMMA) rod, a Polytetrafluoroethylene (PTFE) tube, a PTFE rod, and a Polyimide (PI) tube. It is important to note that the thin PI tube can be clearly resolved only in Fig. 3(b) reconstructed using the speckle scanning approach even though the wall thickness is only 23 μm, while it is difficult to resolve it using the speckle tracking technique. Moreover, the speckle scanning technique produces better reconstruction quality as can been seen from Fig. 3(b). As demonstrated in Fig. 2, such improvement can be attributed to the higher angular sensitivity and

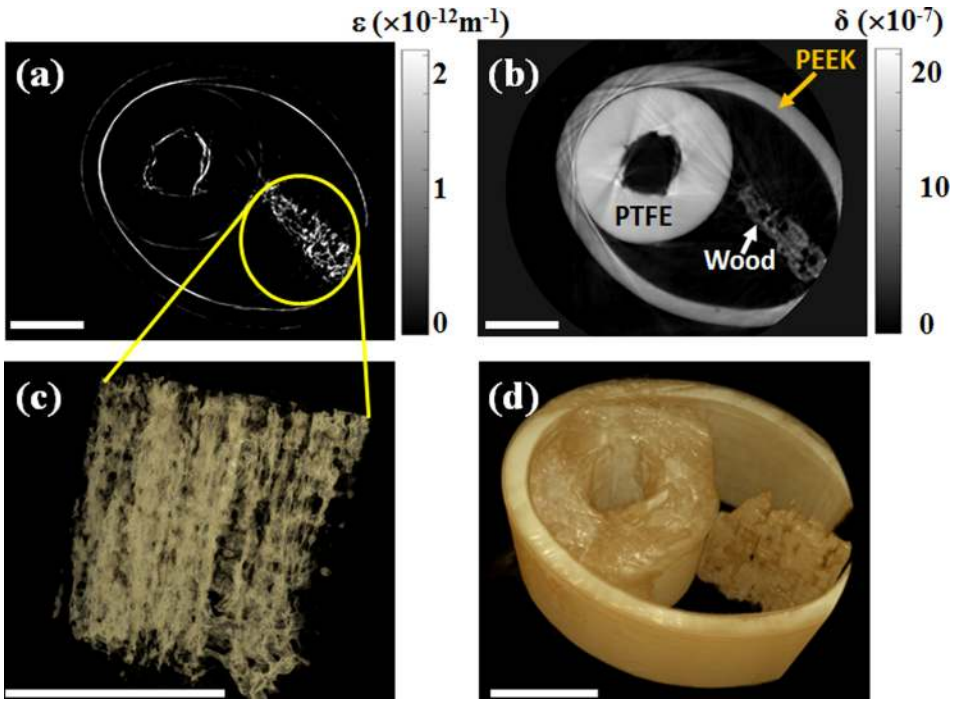

FIG. 4. Dark-field (a) and phase contrast (b) axial slices and 3D rendering of dark-field (c) and phase (d) tomographic reconstruction of tube and wood phantom using single direction speckle scanning approach. The scale bar in the bottom left corner is 1 mm long.

reduced artefact of phase gradients. The quantitative values for X-ray refractive index decrement (δ) was determined by positioning the peak of histogram of the surrounding material (for this case air) to its literature value ($\delta_{air} = 1.15 \times 10^{-9}$).[36] The retrieved δ values for PTFE and PMMA are 1.95×10^{-6} (± 0.01) and 1.19×10^{-6}(± 0.02), respectively, and they are in good agreement with their theoretically calculated values. However, the δ value of PEEK is 0.98×10^{-6} (± 0.02), which is slightly smaller than the ideal case.

To verify the above theoretical deduction for quantitative dark-field tomography, we also investigated another phantom composed of PEEK and PTFE tubes, and a piece of wood. The reconstructed axial slice of dark-field and phase is shown in Figs. 4(a) and 4(b), respectively. The soft materials, such as PEEK and PTFE, show substantial enhanced contrast in the phase slice, while they can hardly be seen in the corresponding dark-field map. It may be noted that the edges of the tubes show a strong dark-field signal because of the second-order differential phase-contrast.[37] As expected, a significant scattering power is clearly observed due to the porous nature of wood. Thanks to the high resolution offered by the proposed tomographic technique, the subtle details of the scattering power distribution are clearly seen in the 3D rendering of dark-field tomographic reconstruction of wood (Fig. 4(c)). In contrast to the dark-field signal, there is a clear difference in contrast between PEEK, PTFE tubes, and wood in the phase tomographic map (Fig. 4(d)). If one looks more closely, the features on the edge of the PTFE tube can be clearly observed. This study demonstrates that distinct and supplementary information can be obtained from phase-contrast and dark-field contrast tomographic images, which are produced simultaneously by the proposed technique.

We have demonstrated the advantage of the single directional speckle scanning technique compared to the speckle tracking technique by imaging a fish eyeball and two phantoms representative of biological and materials science applications, respectively. In particular, a quantitative theoretical basis for dark-field has been established, and the single directional speckle scanning technique has been extended to generate high resolution dark-field CT images. In addition, the data acquisition time can also be reduced if the experiments are carried out on high brilliance undulator beamlines and by using high efficiency X-ray cameras. Since complementary information can be obtained from dark-field and phase signal, the proposed technique will be potentially useful for comprehensive study of internal structure or micro-cracks and defects within the volume of a material. Importantly, no extra dose is delivered since both signals are extracted simultaneously from a single data set. Furthermore, due to a simple experimental setup and moderate requirement on X-ray beam quality, the proposed speckle based phase and dark-field CT technique is expected to find widespread application in both biomedical imaging and non-destructive materials testing.

This work was carried out with the support of Diamond Light Source, Ltd. UK. The authors are grateful to Mark Basham and Robert Atwood for using Diamond tomography software, and Ian Pape and Vo Nghia for their technical assistance during the experiments.

[1]F. Pfeiffer, M. Bech, O. Bunk, P. Kraft, E. F. Eikenberry, C. Bronnimann, C. Grunzweig, and C. David, Nat. Mater. **7**(2), 134–137 (2008).
[2]F. Pfeiffer, T. Weitkamp, O. Bunk, and C. David, Nat. Phys. **2**(4), 258–261 (2006).
[3]E. Pagot, P. Cloetens, S. Fiedler, A. Bravin, P. Coan, J. Baruchel, J. Härtwig, and W. Thomlinson, Appl. Phys. Lett. **82**(20), 3421–3423 (2003).
[4]A. Olivo and R. Speller, Appl. Phys. Lett. **91**(7), 074106–074103 (2007).
[5]C. David, B. Nohammer, H. H. Solak, and E. Ziegler, Appl. Phys. Lett. **81**(17), 3287–3289 (2002).
[6]A. Momose, S. Kawamoto, I. Koyama, Y. Hamaishi, K. Takai, and Y. Suzuki, Jpn. J. Appl. Phys., Part 2 **42**, L866–L868 (2003).
[7]S. W. Wilkins, T. E. Gureyev, D. Gao, A. Pogany, and A. W. Stevenson, Nature **384**(6607), 335–338 (1996).
[8]F. A. Vittoria, M. Endrizzi, P. C. Diemoz, U. H. Wagner, C. Rau, I. K. Robinson, and A. Olivo, Appl. Phys. Lett. **104**(13), 134102 (2014).
[9]F. Pfeiffer, O. Bunk, C. David, M. Bech, G. L. Duc, A. Bravin, and P. Cloetens, Phys. Med. Biol. **52**(23), 6923 (2007).
[10]T. Weitkamp, A. Diaz, C. David, F. Pfeiffer, M. Stampanoni, P. Cloetens, and E. Ziegler, Opt. Express **13**(16), 6296–6304 (2005).
[11]P. Cloetens, W. Ludwig, J. Baruchel, D. V. Dyck, J. V. Landuyt, J. P. Guigay, and M. Schlenker, Appl. Phys. Lett. **75**(19), 2912–2914 (1999).
[12]B. S. Magdalena, P. M. Thomas, I. Konstantin, D. S. Robert, and O. Alessandro, Phys. Med. Biol. **59**(5), N1 (2014).
[13]A. Momose, T. Takeda, Y. Itai, and K. Hirano, Nat. Med. **2**(4), 473–475 (1996).
[14]M. Bech, O. Bunk, T. Donath, R. Feidenhans'l, C. David, and F. Pfeiffer, Phys. Med. Biol. **55**(18), 5529 (2010).
[15]A. Sarapata, M. Ruiz-Yaniz, I. Zanette, A. Rack, F. Pfeiffer, and J. Herzen, Appl. Phys. Lett. **106**(15), 154102 (2015).
[16]P. Coan, A. Bravin, and G. Tromba, J. Phys. D: Appl. Phys. **46**(49), 494007 (2013).
[17]B. Alberto, C. Paola, and S. Pekka, Phys. Med. Biol. **58**(1), R1 (2013).
[18]S. Schleede, F. G. Meinel, M. Bech, J. Herzen, K. Achterhold, G. Potdevin, A. Malecki, S. Adam-Neumair, S. F. Thieme, F. Bamberg, K. Nikolaou, A. Bohla, A. Ö. Yildirim, R. Loewen, M. Gifford, R. Ruth, O. Eickelberg, M. Reiser, and F. Pfeiffer, Proc. Natl. Acad. Sci. U.S.A. **109**(44), 17880–17885 (2012).
[19]I. Zanette, M. Bech, A. Rack, G. Le Duc, P. Tafforeau, C. David, J. Mohr, F. Pfeiffer, and T. Weitkamp, Proc. Natl. Acad. Sci. U.S.A. **109**(26), 10199–10204 (2012).
[20]P. Zhu, K. Zhang, Z. Wang, Y. Liu, X. Liu, Z. Wu, S. A. McDonald, F. Marone, and M. Stampanoni, Proc. Natl. Acad. Sci. U.S.A. **107**(31), 13576–13581 (2010).
[21]Y. Zhao, E. Brun, P. Coan, Z. Huang, A. Sztrókay, P. C. Diemoz, S. Liebhardt, A. Mittone, S. Gasilov, J. Miao, and A. Bravin, Proc. Natl. Acad. Sci. U.S.A. **109**(45), 18290–18294 (2012).
[22]A. Snigirev, I. Snigireva, V. Kohn, S. Kuznetsov, and I. Schelokov, Rev. Sci. Instrum. **66**(12), 5486–5492 (1995).
[23]K. S. Morgan, D. M. Paganin, and K. K. W. Siu, Appl. Phys. Lett. **100**(12), 124102–124104 (2012).
[24]S. Berujon, E. Ziegler, R. Cerbino, and L. Peverini, Phys. Rev. Lett. **108**(15), 158102 (2012).
[25]H. Wang, S. Berujon, J. Herzen, R. Atwood, D. Laundy, A. Hipp, and K. Sawhney, Sci. Rep. **5**, 8762 (2015).
[26]S. Berujon, H. Wang, and K. Sawhney, Phys. Rev. A **86**(6), 063813 (2012).
[27]T. Zhou, I. Zanette, M.-C. Zdora, U. Lundström, D. H. Larsson, H. M. Hertz, F. Pfeiffer, and A. Burvall, Opt. Lett. **40**(12), 2822–2825 (2015).
[28]H. Wang, Y. Kashyap, and K. Sawhney, Sci. Rep. **6**, 20476 (2016).
[29]K. Gocha, G. B. Jovan, C. Dean, A. A. Mark, Y. Yongyi, Z. Zhong, and N. W. Miles, Phys. Med. Biol. **51**(2), 221 (2006).
[30]Z.-T. Wang, K.-J. Kang, Z.-F. Huang, and Z.-Q. Chen, Appl. Phys. Lett. **95**(9), 094105 (2009).
[31]M. Guizar-Sicairos, S. T. Thurman, and J. R. Fienup, Opt. Lett. **33**(2), 156–158 (2008).
[32]J. W. Goodman, *Introduction to Fourier Optics*, 3rd ed. (Roberts & Company Publishers, 2005).
[33]H. Wang, Y. Kashyap, and K. Sawhney, Phys. Rev. Lett. **114**(10), 103901 (2015).
[34]H. Wang, Y. Kashyap, and K. Sawhney, Opt. Express **23**(18), 23310–23317 (2015).
[35]K. J. S. Sawhney, I. P. Dolbnya, M. K. Tiwari, L. Alianelli, S. M. Scott, G. M. Preece, U. K. Pedersen, and R. D. Walton, AIP Conf. Proc. **1234**(1), 387–390 (2010).
[36]B. L. Henke, E. M. Gullikson, and J. C. Davis, At. Data Nucl. Data Tables **54**(2), 181–342 (1993).
[37]Y. Yang and X. Tang, Med. Phys. **39**(12), 7237–7253 (2012).